Protein Trapping in Plasmonic Nanoslit and Nanoledge Cavities: The Behavior and Sensing

By: Zheng Zeng, Xiaojun Shi, Taylor Mabe, Shaun Christie, Grant Gilmore, Adam W. Smith, and Jianjun Wei

Z. Zeng, X. Shi, T. Mabe, S. Christie, G. Gilmore, A. Smith, J. Wei, Protein Trapping in Plasmonic Nanoslit and Nanoledge Cavities: The Behavior and Sensing, *Analytical Chemistry*, **2017**, 89 (10), 5221–5229. DOI: 10.1021/acs.analchem.6b04493

Abstract:

A novel plasmonic nanoledge device was presented to explore the geometry-induced trapping of nanoscale biomolecules and examine a generation of surface plasmon resonance (SPR) for plasmonic sensing. To design an optimal plasmonic device, a semianalytical model was implemented for a quantitative analysis of SPR under plane-wave illumination and a finite-difference time-domain (FDTD) simulation was used to study the optical transmission and refractive index (RI) sensitivity. In addition, total internal reflection fluorescence (TIRF) imaging was used to visualize the migration of fluorescently labeled bovine serum albumin (BSA) into the nanoslits; and fluorescence correlation spectroscopy (FCS) was further used to investigate the diffusion of BSA in the nanoslits. Transmission SPR measurements of free prostate specific antigen (f-PSA), which is similar in size to BSA, were performed to validate the trapping of the molecules via specific binding reactions in the nanoledge cavities. The present study may facilitate further development of single nanomolecule detection and new nanomicrofluidic arrays for effective detection of multiple biomarkers in clinical biofluids.

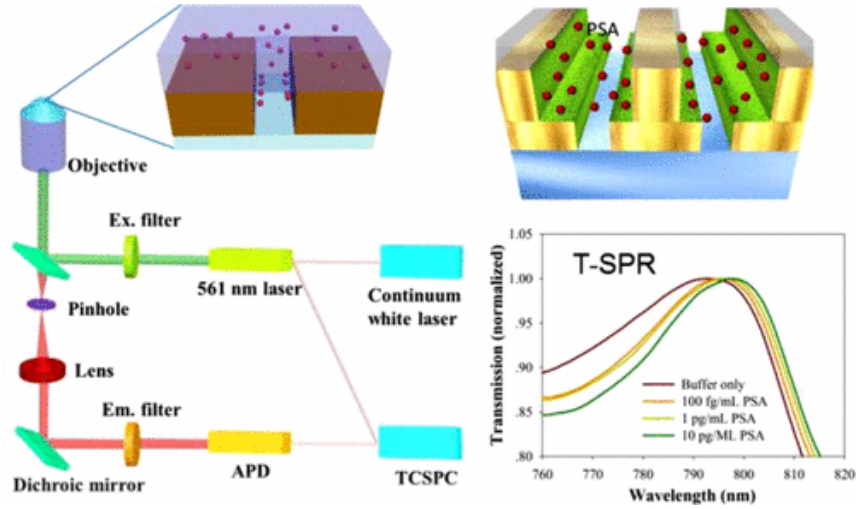

Keywords: surface plasmon resonance (SPR) | nanomolecule | finite-difference time-domain (FDTD)

Article:

The latest advances in manipulation, trapping, alignment, and separation of molecules embrace fields as diverse as quantum optics, soft condensed-matter physics, biophysics, and clinical medicine.[1, 2] Many technologies, whether active techniques (external fields) or passive ones (hydrodynamic interactions or inertial effects),[3-7] have been developed to counter and trap the Brownian motion of small molecules in solution. However, confinement of nanomolecules in the absence of external fields and visualizing the dynamics of nanomolecules in the nanometric-sized objects remain challenging. Total internal reflection fluorescence (TIRF) imaging could be a potential solution to these challenges, since the incident light creates a thin surface electromagnetic field (around 100 nm) enabling the detection of only the labeled fluorophores that are within the nanometric depth. In addition, fluorescence correlation spectroscopy (FCS), a time-resolved fluorescence method, could analyze the temporal fluctuations due to diffusion of fluorophores in and out of a nanostructure. This is done by utilizing a confocal laser beam with ~0.2 fL of volume to detect the diffusion of particles crossing the laser focus.[8-11] The recorded fluorescence fluctuations are then correlated for analysis, directly yielding information about the mobility of the diffusing particles.[12] Recently, FCS has been applied to measure tracer diffusion in nanofluids[13] and to investigate membrane dynamics through nanoapertures.[14]

For practical purposes, stable nanomolecule trapping and detection have received intense attention because of the focus on *in vitro* detection of target molecules. This approach makes use of the versatility of optical sensing and the convenience of nanoplasmonic-chip-based device integration with different nanostructures, including pores, channels, and slits.[15-18] The useful phenomenon, which underlies the ability of such nanoapertures to light with high efficiency, is transmission surface plasmon resonance (T-SPR), which has sparked an interest in deeply understanding the fundamentals of T-SPR physics,[19-21] encouraging researchers to explore new ways for nanoscale molecule trapping, and creating novel, robust nanoscale sensors.[22-25] It has been recently understood that nanoplasmonic devices, with strong plasmon excitation and stable convective trapping of nanomolecules, can be especially suitable for applications if they incorporate real metals with a finite conductivity,[26] sufficiently high intensity of light scattering,[27] extraordinary optical transmission (EOT),[28, 29] high refractive index (RI) sensitivity at the perforated metal films,[30] and a single nanometer-scale pore for single molecule thermodynamics and kinetics.[31]

Here, we present and investigate novel nanoledge aperture structures for convective molecular trapping and implement a quantitative analysis of surface plasmon (SP) generation using an earlier developed semianalytical model.[32] In addition, we perform numerical simulations using a finite-difference time-domain (FDTD) method to model optical transmission spectra and RI sensitivity as a function of the nanoledge device geometrical parameters.[33] Experimentally, we used the techniques of TIRF to visualize the migration of Texas Red-labeled bovine serum albumin (TxR-BSA) molecules into the nanoslits and FCS to detect its dynamics in nanoslits with different widths. Later, the molecular trapping and sensing in the nanoledge structure were validated using a fabricated subwavelength gold-film nanoledge device which was integrated

with a microfluidic channel allowing us to measure the SPR induced optical transmission, RI sensitivity, and detect the specific binding events of free prostate specific antigen (f-PSA) biomarkers to the gold surfaces functionalized with antibody of f-PSA in the nanoslit cavities.

Methods and Materials

Semianalytical Analysis of SP Generation and FDTD Simulations. The SP scattering coefficients and efficiencies at the slit apertures can be determined from analysis of diffraction of bounded SP modes that originates on the flat interfaces surrounding the slits in order to study nanoledge geometries that are of interest in practice and consider the geometric diffraction with the bounded SP modes launching on the flat interfaces surrounding the slits. Moreover, FDTD simulations reiterated the previous study by adding additional 10 nm SiO_2 film at the top of Au layer.[32] Refractive index of the SiO_2 film used in calculations was equal to 1.41. More details of the semianalytical model analysis applied to the SiO_2 film topped nanoledge devices and results are provided in Supporting Information (SI).

Fabrication of Ledged Flow-through Nanoplasmonic Device. Standard photolithography was used to pattern soda lime glass slides (75 × 25 mm, Globe Scientific). Slides were fully covered with a 600 nm layer of aluminum by DC sputtering (PVD 75, Kurt Lesker). A dark field mask was designed in AutoCAD and printed on a transparency film using a 25400 dpi printer. The mask design, shown in Figure S5, consisted of a flow channel with two dam structures, each of which was 30 μm wide. Shipley 1827 positive photoresist was applied to hexamethyldisilazane (HMDS) treated glass slides by spin coating. The slides were then exposed with deep UV using an OAI 8800 mask aligner and developed with Microposit MF-321 developer. The aluminum layer was wet etched using Aluminum Etchant Type A (Transene Company) and the glass was then wet or dry etched to yield an isotropic or anisotropic dam structure, respectively. This process is fully outlined in Figure S6. The patterned glass slides were covered with 2 nm Ti, 150 nm Au, and 10 nm of SiO_2 by electron beam evaporation (PVD75, Kurt Lesker). Focused ion beam milling (Zeiss, Auriga) was used to introduce the nanoledge structures atop the 30 μm dams. A slit, 50 nm wide, was milled completely through the SiO_2 and gold layers, followed by a 280 nm wide ledge that was milled through the SiO_2 and partially though the gold layer. The nanoledge channel was completely aligned with the direction of microchannels. The device was then enclosed using a poly(dimethylsiloxane) (PDMS) flow channel, which was also fabricated using standard lithographic techniques.[34]

Total Internal Reflection Fluorescence (TIRF) Imaging. Nanoslits were fabricated by FIB on a glass coverslip. The coverslip soaked in detergent solution and IPA/water (50:50) accordingly. The coverslip was rinsed with excess Type I water and dried under a nitrogen stream. Ozone plasma was used to further clean the surface of the coverslip. The coverslip was assembled in an AttoFluor sample chamber. TIRF imaging was recorded on a Nikon Eclipse Ti inverted microscope equipped with a 2 mW 488 nm diode laser (85-BCD-020-115, Melles Griot) and 100× TIRF objective (NA 1.47 oil, Nikon Corp., Tokyo, Japan). Fluorescence signal was collected by an EM-CCD camera (Evolve 512, Photometrics) with a frame rate of 12 frames per second. The raw images were processed by ImageJ and the Mosaic Particle Tracker plugin for ImageJ was used to perform background subtraction and deconvolution of the raw images.

Fluorescence Correlation Spectroscopy (FCS). FCS measurements were performed on a customized Nikon Eclipse Ti inverted microscope. Briefly, a 561 nm laser beam was picked out by 561 nm ± 20 nm dichroic mirror from a pulsed continuum white light laser (9.7 MHz, SuperK NKT Phontonics) and focused on the sample through a 100× TIRF objective (oil, NA 1.49, Nikon). The laser beam was carefully placed at the nanoslit position. The emitted photons were collected through the same objective and directed to a single photon avalanche diode (SPAD) detector (Micro Photon Devices). Photons collected by the detector were recorded with a time-correlated single photon counting (TCSPC) card (Picoharp 300) that was synchronized with the white light laser source. Five times of 30 s measurements were performed at the same spot of each nanoslit and were averaged in the correlation analysis. Correlation analysis was then performed on a computer with a custom-written Matlab script.

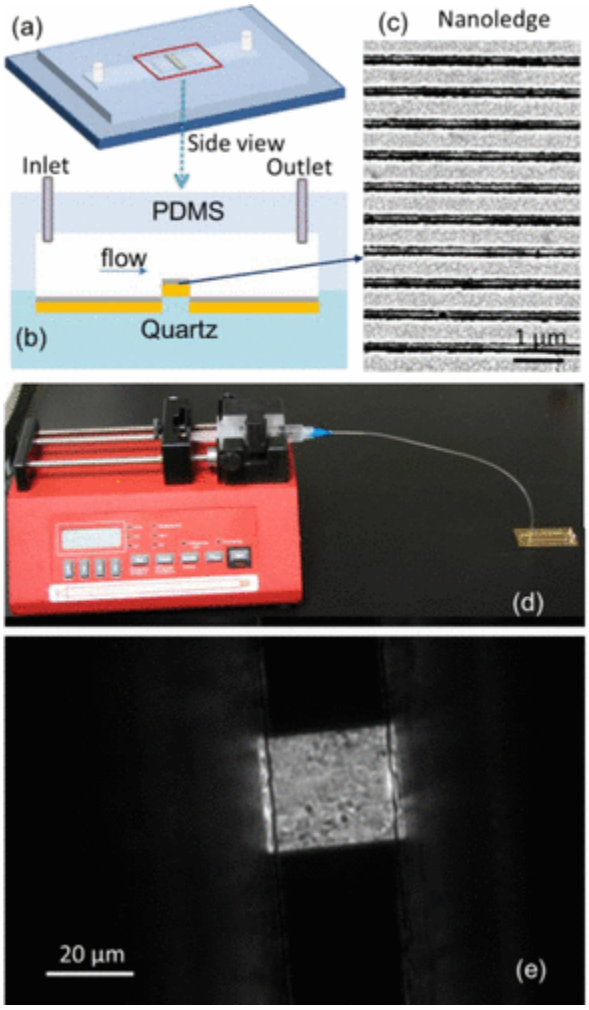

Figure 1. (a) Schematic illustration of the interface between the nanoledge array at the quartz chip and PDMS microfluidic channel, (b) side view of the microchannel, and (c) a SEM image of the nanoledge array. (d) Microfluidic syringe pump connected to the PDMS microfluidic channel to control the flow rates for sample delivery. (e) Bright field image of the nanoledge array cross the "dam" with a 60× objective.

Preparation of Immobilized mAb Detector at Nanoplasmonic Gold Surfaces. The approach, combining a self-assembled monolayer (SAM) and a cross-link reaction, was used for the immobilization of a monoclonal antibody (mAb) of f-PSA.[35] The gold-coated chips were first cleaned with O_2 plasma (South Bay Technologies PC2000 Plasma Cleaner) for 15 min. Then, the chips were processed overnight by a SAM using incubation in a mixture of 1 mM 11-mercaptodecanoic acid (HSC10COOH, Aldrich) and 8-mercapto-octanol (HSC8OH, Aldrich) in absolute ethanol solution with 1:2 mole ratio. After that, the SAM was activated by incubation in a 10 mM phosphate buffer solution (pH 7.0) with 0.5 mM of EDC/NHS for 2 h. The activated SAM was rinsed with 10 mM PBS and immediately moved to a freshly prepared 10 mM PBS containing 10 μg/mL of the detector mAb for a subsequent 4 h incubation. Then, the chip was rinsed with the PBS again and was dipped into a 0.2 M glycine PBS solution for 10 min in order to deactivate the remaining active sites at the SAM. The immobilized mAb was then ready for f-PSA binding.

Experimental Setup for Flow Control. A New Era pump system (NE-300) was used to control the flow rate to inject the sample solution to the microfluidic channel where the nanoledge array located in the center of the channel. Figure 1 shows the device sketch and an image of an actual device topped with a PDMS microfluidic channel and connection with the syringe pump for flow sample injection and flow rate control.

Results and Discussion

Two types of nanoledge structures, as shown in Figure 2a,b, have been investigated. One nanoledge structure has an exposed gold surface and the other has a SiO_2 film (~10 nm thickness) coated atop the gold. The nanoledge array will allow for geometry induced nanoscale particle (e.g., proteins) trapping and plasmonic sensing using the metal film in the nanoledge cavity via T-SPR measurements. It is expected that the device, with the additional SiO_2 film, will allow for in-cavity detection with enhanced sensitivity.[36, 37] The in-plane nanoledge array platform is different from the well-recognized EOT nanohole flow-through pattern[38, 39] in which the sample flow direction is parallel to the incident light and normal to the chip plane. The nanoledge platform offers a solution-flow that is parallel to the chip plane and perpendicular to the incident light for plasmonic transmission in sensing applications. Hence, when used in clinical applications, like protein detection in whole blood or tissue lysates, it potentially provides a simple way to integrate with the microfluidic channels for nanometric-sized protein delivery to the nanoledge cavities, while larger particles (e.g., cells, or biofragments) simply flow over the top of the nanoledge array. This allows for minimizing or avoiding the interference from nonspecific binding of cells or biofragments.

Semianalytical Analysis of SP Generation and FDTD Simulation. Based on our recent fundamental work[32] and the SP generation results of the open nanoledge structure, the optimal geometry of the plasmonic nanoledge slit has 280–300 nm open width and 50 nm bottom slit width. To develop the nanoledge structure for investigating the trapping of molecules by the T-SPR measurement, we performed a proof-of-principle calculation of the SP generation at the flat interface of the nanoledge structures with and without the SiO_2 layer using a semianalytical approach.[32, 40] A comparison of the semianalytical decomposition analysis of SP generation efficiency, which is defined as the rate of surface plasmon polariton (SPP) launching,

propagation and scattering by matching the continuous electromagnetic fields quantities at the interface,[26, 32] between the two different nanoledge structures are shown in Figure 2a,b. Predicted SP generation efficiencies e were calculated as functions of the nanoledge widths (top 280 nm and bottom 50 nm) and RIs (n_1 = 1.41, n_2 = n_3 = bulk media RI, n_4 = stochastic RI) caused by a plane light wave (λ = 600 nm) scattering at normal incidence to the nanoledge structure (details in SI). We found that when the RI of bulk media changed from 1.0 to 1.2, the absolute value of the total SP generation efficiency, Δ(e1 + e2 + e3), decreased from 0.08 for the nanoledge structure with SiO_2 to the value of 0.06 for the nanoledge structure without SiO_2.

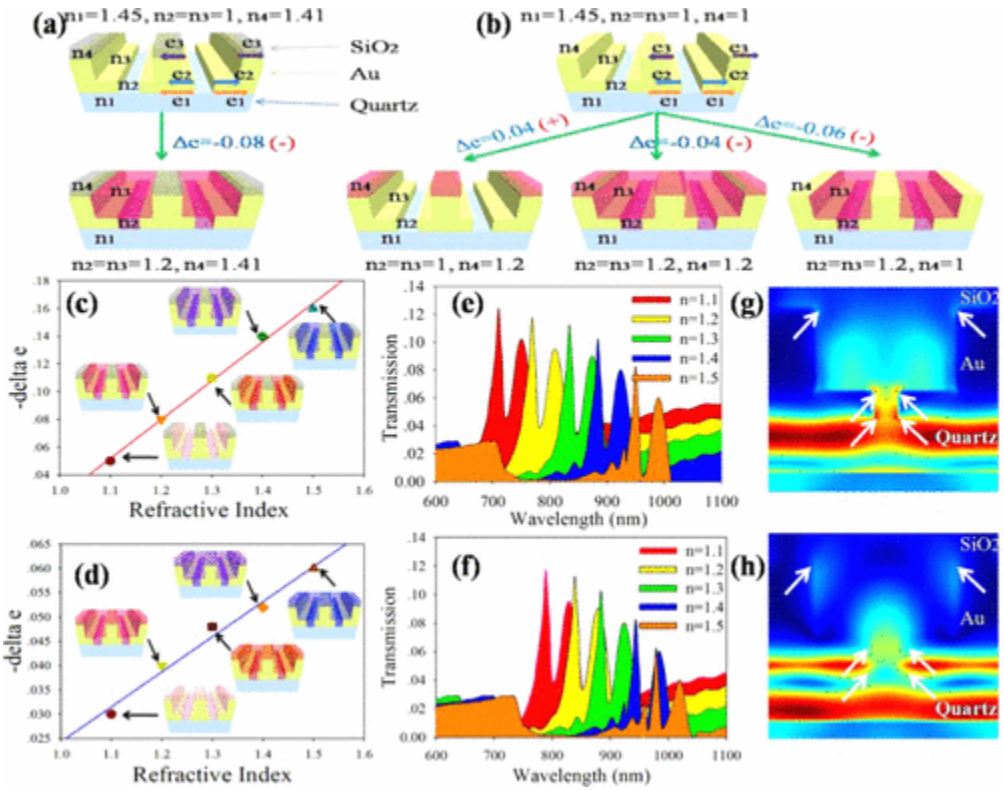

Figure 2. SP generation efficiency change, Δ(e1 + e2 + e3), for the nanoledge geometry of 280–50 nm with on-top SiO_2 layer (a) and without on-top SiO_2 layer (b) for the bulk media RI ranging from 1.0 to 1.2. The SP generation efficiency for the nanoledge with on-top SiO_2 layer (c) and without on-top SiO_2 layer (d) as the surrounding medium RI increases from 1.1 to 1.5. The calculated transmission spectra with on-top SiO_2 layer (e) and without on-top SiO_2 layer (f) as the surrounding medium RI increases from 1.1 to 1.5. The TE field distribution (g) and TM field distribution (h) of the 280–50 nm nanoledge with on-top SiO_2 layer.

It has been found that the EOT peak shift, due to a weakened SP generation efficiency, correlates with a red shift of the optical transmission peak resulting from a coupling of dielectric changes with nanoledge geometry parameters.[32] The in-gap surfaces of the nanoledge structure have a larger RI sensitivity than the top-of-gap surface mode; therefore, the nanoledge structure with SiO_2 demonstrates higher sensitivity to the binding events when the molecule is trapped into the nanoledge gap. As the RI of the surrounding media is increased up to 1.5, this effect is further elucidated by an almost 3-fold decrease of the total SP generation efficiency. This value

decreases from 0.16 to 0.06 for nanoledge structures with and without SiO_2 atop, respectively (Figure 2c,d).

In concert with the semianalytical analysis, Figure 2e,f summarizes the transmission spectra computed by a numerical 3D FDTD method for two selected nanoledges for RIs of a variety of surrounding medium from 1.1 to 1.5. Note that the setup of the FDTD method was similar to that of a previous study[32, 33] except the topped 10 nm SiO_2 surface layer. The peak wavelength shift of the nanoledge structure with SiO_2 (ca. 595 nm/RIU, Figure S1) was obtained and larger than that of the nanoledge structure without SiO_2 (ca. 556 nm/RIU[32]).

We calculated the transverse electric (TE) and transverse magnetic (TM) modes for the nanoledge structure topped with SiO_2 (Figure 2g,h). Using a Drude dielectric function for bulk Au,[33, 41] we analyzed Au interfaces with quartz, air, and SiO_2. It was found that the enhanced electromagnetic fields were located near in-gap surfaces for all three interfaces and those fields were higher in magnitude than in the nanoledge structure without SiO_2. This finding was further confirmed by computing the TE wave propagation through the simulation volume of 280–50 nm nanoledge system with SiO_2, as shown in Figure S2. The simulation results prove the higher SP generation and enhanced sensitivity of the nanoledge structure topped with SiO_2 for detection of RI changes in the nanoledge gap area.

TIRF and FCS Studies of Protein Behavior. To study the diffusion of nanomolecules in the nanoledge structure, two kinds of nanoslit array chips were fabricated. These had slit widths of 100 or 300 nm and both had a period of 5.4 μm, as Figure S3. The 100 nm array can be located and observed with reflection interference contrast microscopy (RICM) and transmitted light microscopy (TLM; Figure 3a,b). Since the size of the nanoslits is below the wavelength of visible light, diffracted features of the nanoslits were obtained. Once the nanoslits were located, a 561 nm laser was sent through the objective to allow TIRF imaging of the TxR-BSA molecules in the nanoslits. Note that the TIRF incident laser generates an evanescent excitation field, which decays exponentially from the substrate interface and penetrates to a depth of approximately 100 nm into the sample medium. Because the height of the nanoslits was 150 nm, the fluorescent signals picked up by TIRF imaging would be only due to the emission of fluorophores within the nanoslits (Figure 3 left panel). At first, the nanoslits appear to be totally nonfluorescent under TIRF imaging. Upon adding TxR-BSA to the medium, weak fluorescent signal was detected at the location of the nanoslits after 24 s (Figure 3c), indicating that TxR-BSA molecules entered the nanoslits. The fluorescent signal increased with longer observation time (Figure 3d,e) and finally reached a steady state. The TIRF imaging observation clearly demonstrates that TxR-BSA can diffuse into the 100 nm nanoslits. The gradual increase of the fluorescent signal suggests that the diffusion is driven by a concentration gradient and short-range energetic interactions at higher confinement grades.

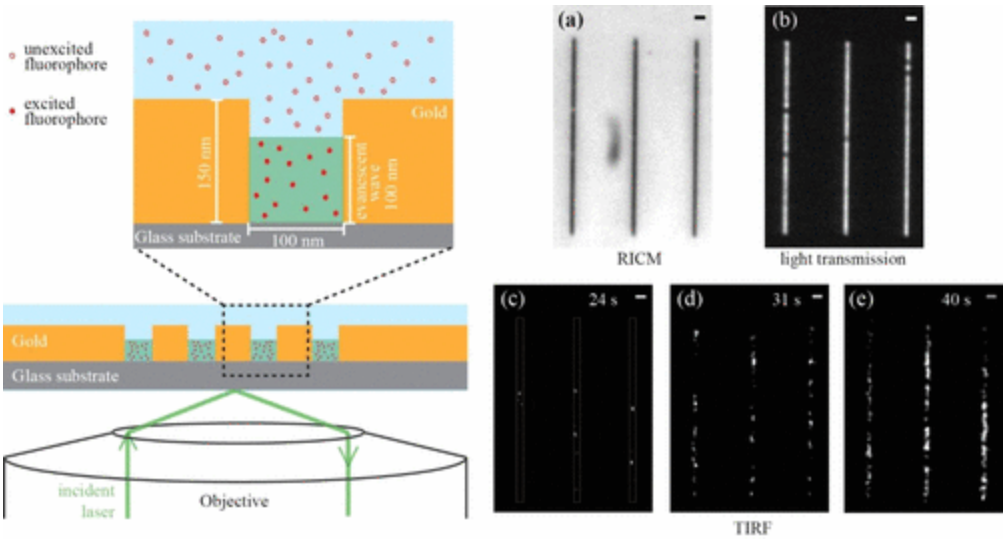

Figure 3. Left: schematic diagram of TIRF imaging. TIRF incident laser creates an evanescent wave that only excites fluorophores within 100 nm range from the glass substrate. With a slit depth of 150 nm, only those fluorophores that enter the nanoslit will be excited and observed. Right: (a) RICM and (b) TLM image of 100 nm nanoslits. (c–e) TIRF images of TxR-BSA diffusion into the nanoslits at time points of 24, 31, and 40 s, respectively. The density and intensity of fluorescence increase along with time, indicating that TxR-BSA molecule can diffuse into the nanoslits. A video clip of the process is available in the SI. The positions of nanoslits were indicated by white boxes. All scale bars are 1 μm.

The diffusion of TxR-BSA molecules was further studied by FCS (Figure 4a), which collects time-resolved fluorescence fluctuation caused by diffusion of fluorophores in and out of a confocal laser beam.[42] The detection volume of the laser beam is diffraction limited, about 1.2 femtoliter, which makes FCS a single molecule sensitive method. The information on the diffusion of the molecules, which is concealed in the fluorescence fluctuation can be extracted by correlation:[43, 44]

$$G(\tau) = \frac{\langle \delta F(t+\tau)\delta F(t)\rangle}{\langle F(t)\rangle^2} \tag{1}$$

where $\langle\ \rangle$ stands for a time average, $F(t)$ is fluorescence intensity at time t, and $\delta F(t) = F(t) - \langle F(t)\rangle$. The inflection point of the resulting autocorrelation function (ACF) curve represents the average dwell time (τ_D) of the diffusive molecule (Figure 4b). The τ_D of three-dimensional diffusion can be obtained by fitting the ACF curve with the three-dimensional diffusion model:

$$G(\tau) = G(0)\frac{1}{\left(1+\frac{\tau}{\tau_D}\right)}\frac{1}{\sqrt{1+\left(\frac{\omega_0}{z_0}\right)^2\frac{\tau}{\tau_D}}} \tag{2}$$

where ω_0/z_0 is the ration of lateral and axial waist of the detection volume. The term ω_0/z_0 is used to allow a float in the fitting process and only affects the fitting at the end of the decay. Uncertainty in ω_0/z_0 does not bias τ_D by more than a couple of percent. Once τ_D and ω_0 are

calibrated, the diffusion coefficient (D, typically reported in μm^2/s) of the molecule can be calculated using

$$\tau_D = \frac{\omega_0^2}{4D} \tag{3}$$

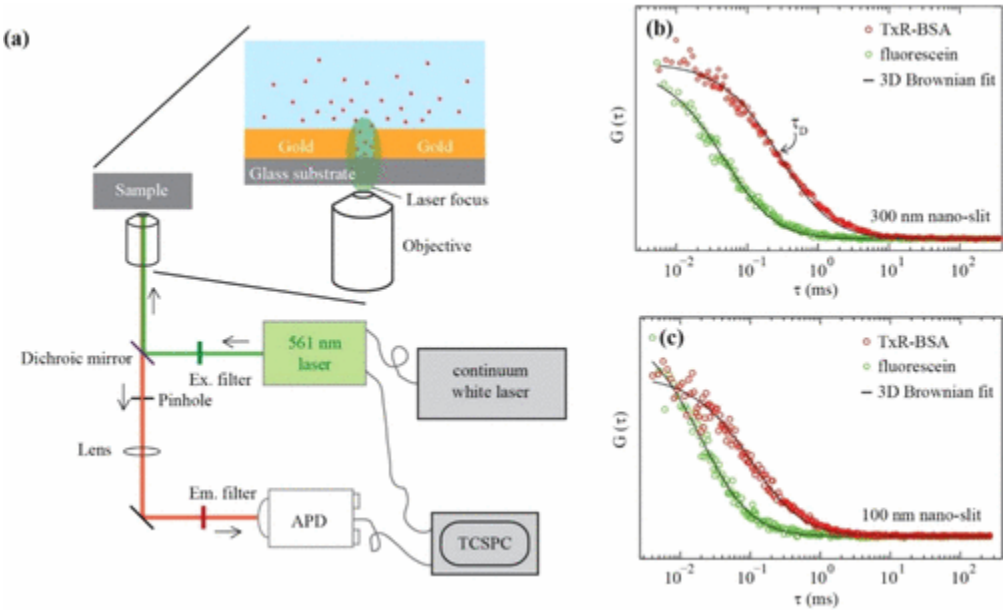

Figure 4. (a) Diagram of FCS setup for measuring protein diffusion in the nanoslits. The effective detection area, which is defined by the size of the nanoslits, is smaller than the diffraction limited confocal detection area (laser focus). Sample ACF curves of fluorescein and TxR-BSA diffusion in the 300 nm nanoslits (b) and in the 100 nm nanoslits (c). The inflection point of the ACF curve indicates the average dwell time (τ_D) of fluorescent molecules within the detection volume.

As illustrated in Figure 4a, the confocal laser beam was sent through the nanoslits to excite and detect fluorophores in the nanoslits. Since the size of the nanoslits is smaller than the diffraction limited laser beam, the actual detection volume is limited by the geometry of the nanoslits. A three-dimensional model is not perfectly fit for a slit structure to obtain the exact shape and size of the detection volume where the molecule is laterally confined; however, a standard method using a molecule with known diffusion coefficient can be used to estimate the so-called effective detection volume. In order to quantify the lateral detection area, a standard dye molecule, fluorescein, with known D (430 μm^2/s) was used.[45] By measuring the average dwell time (τ_D) of fluorescein in the nanoslits, the effective detection area (A_{eff}) can be estimated using

$$\tau_D = \frac{A_{eff}}{D} \tag{4}$$

The calibrated A_{eff} was then used for D calculation for BSA diffusion with the τ_D extracted from ACF curve. Figure 4b,c show examples of ACF curves of fluorescein motion in 300 and 100 nm nanoslits. The average dwell time (τ_D) of fluorescein in the 300 and 100 nm nanoslits is 0.052

and 0.028 ms, respectively. Based on the τ_D, the calculated A_{eff} for 300 and 100 nm nanoslits is 0.0224 and 0.0120 μm^2. The data are summarized in Table 1.

Table 1. Results Obtained from FCS Measurements

	fluorescien τ_D (ms)	**A_{eff} (μm^2)**	**TxR-BSA τ_D (ms)**	**TxR-BSA D (μm^2/s)**
300 nm nanoslits	0.052 ± 0.002	0.0224 ± 0.001	0.320 ± 0.006	69.9 ± 1.3
100 nm nanoslits	0.028 ± 0.006	0.0120 ± 0.003	0.180 ± 0.001	66.9 ± 0.4

The diffusion of TxR-BSA was measured by FCS as well. As expected, the larger BSA molecule has a slower motion than the fluorescein molecule does. As shown in Figure 4b,c, the ACF curves of TxR-BSA motion shift toward the longer time domain. The τ_D extracted from the ACF curve is 0.320 and 0.180 ms for 300 and 100 nm nanoslits, respectively, and the τ_D of TxR-BSA is one magnitude larger than that of fluorescein. Obviously, the D of TxR-BSA in 300 and 100 nm nanoslits are both around 70 μm^2/s (Table 1). Based on Stokes–Einstein equation:[46]

$$D = \frac{kT}{6\pi r_h \eta} \tag{5}$$

where k is Boltzmann's constant, T is the temperature, r_h is the hydrodynamic radius, and η is the viscosity of the solvent. TxR-BSA molecules have a hydrodynamic radius of ∼3 nm, which agrees with the reported size of BSA protein.[47] This result indicates that the diffusion of TxR-BSA within the two different sized nanoslits is Brownian motion with the same mobility. Combined with TIRF imaging results, the FCS measurements clearly demonstrate that TxR-BSA molecules can diffuse into the nanoslits via concentration gradient and short-range energetic interactions.

Protein f-PSA in Nanoledge Cavities and Sensing. Next, we performed a preliminary study to use the nanoledge structure for plasmonic sensing. We chose f-PSA biomarker for this performance due to its similar protein size with BSA. To detect such nanomolecule trapping experimentally, we employed a technique based on T-SPR spectrum measurements. A setup for flow-through nanoledge array, shown in Figure 1, was established to test the sample at the flow rate of 10 μL/min. Note that the detection of T-SPR is under the condition of steady state of full-flow in the nanoledge slits. In this way, the nanoledge array was functioning as the nanomicrofluidics that can direct sample delivery of analytes to the plasmonic sensing area by nanomolecule migration. The transmission spectra of the nanoledge array chip were measured in air and confirmed the SAM formation and mAb of f-PSA attachment to the nanoplasmonic sensing area in the gap.[35] Figure S4 displays the transmission spectra of the blank, alkanethiol SAM with carboxylic groups, and after mAb immobilization. The later peaks of the transmission were normalized to the maximum transmission of the primary peak, as shown in Figure 5b. The primary peaks of the three spectra were located at 725.4, 731.1, and 746.5 nm for blank, SAM only, and SAM plus mAb, respectively. The red shifts of the primary peak were 5.7 nm for SAM and 15.4 nm for mAb immobilization. Based on the SPR sensing principle, it has been established to determine the relationship between the peak wavelength and the thickness of the added layer using the following equation:[48, 49]

$$\Delta\lambda = m(n_A - n_B)[1 - \exp(-2d_D/l_d)] \tag{6}$$

where Δλ is defined as the peak wavelength shift after the addition of molecule layer to the precedent step modification, m is the RIU sensitivity, d_E is the effective thickness of the existing layer, l_d is the decay length of surface plasmon mode into the dielectric with 110 nm for the nanoledge dimension, and refractive indices of the organic layer is taken to be 1.5 and that of air is 1.0.[50]

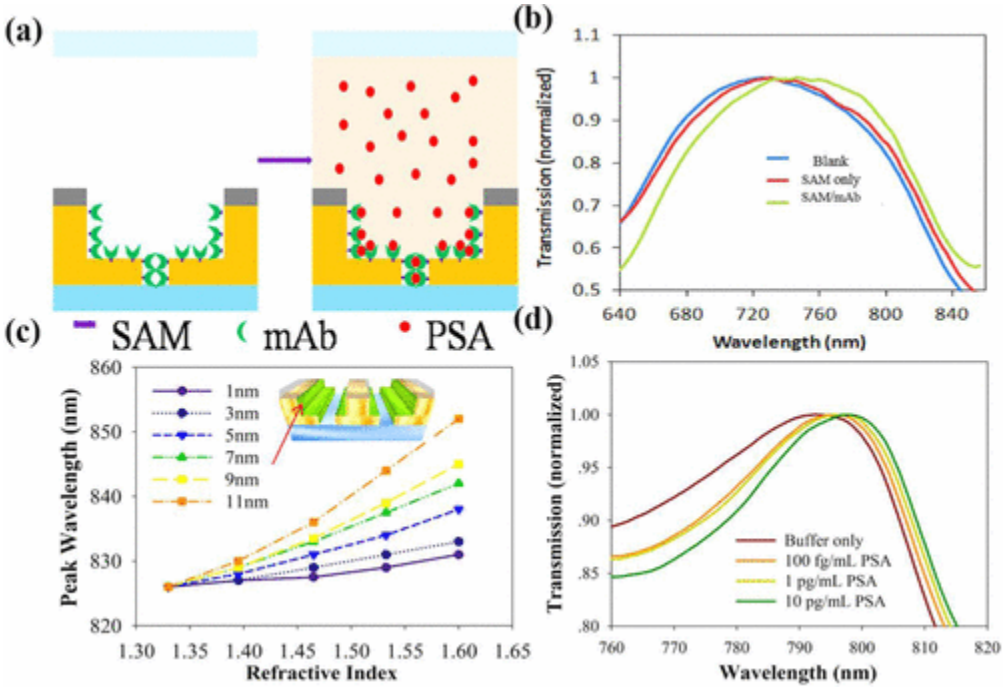

Figure 5. (a) Illustration of the immobilization of the detection antibody (mAb) at the SAM for f-PSA binding. (b) Normalized transmission spectra of the nanoledge device at the primary peak. (c) FDTD calculated peak wavelength for a nanoledge device in which the SAM was located on the walls within the nanochannel for varying thickness values of the SAM as the RI index varied from 1.33 (water) to 1.6 (protein SAM). (d) Normalized spectra of the primary peaks with different concentrations of f-PSA in buffer solution.

Assuming the SAM is packed well at the surface with a thickness of 1.1 nm, one is able to estimate the equivalent molecular thickness of mAb according to the following equation:

$$\frac{\Delta\lambda_{\mathrm{SAM}}}{\Delta\lambda_{\mathrm{SAM=mAb}}} = \frac{1-\exp(-2d_{\mathrm{SAM}}/l_{\mathrm{d}})}{1-\exp(-2d_{\mathrm{SAM+mAb}}/l_{\mathrm{d}})} \tag{7}$$

According to our measured average Δλ, the calculated equivalent thickness of mAb was found to be 1.9 nm. Moreover, the sensitivity was calculated as 576 nm/RIU, which agrees with the FDTD result above. To obtain a more realistic understanding of the device sensitivity to biological interactions through adsorption onto a SAM, a series of FDTD simulations were conducted in which the sidewall RI was changed, while the background RI in the channel remained at 1.33. As we have seen from Figure 5c with the nanoledge device, changing the thickness of the organic layer on the sidewalls of the device resulted in marked red-shifts of peak

wavelengths, since the overall thickness of the organic layer increased, the magnitude of the RI increased as well.

In the end, we moved to the validation of f-PSA, with the same hydrodynamic radius of ~3 nm as BSA,[51] trapping in the nanoledge gap, and binding to the surface in the nanoledge cavities by measuring the peak wavelength shift using T-SPR sensing scheme. It was addressed by the transmission spectra of a series of f-PSA solutions of different concentrations, which were prepared for the f-PSA binding events at the SAM-mAb immobilized at the cavity gold surfaces, starting with the incubation of buffer solution and increasing f-PSA concentration from 0.1 to 10 pg/mL. Figure 5d shows the primary peak also has a red shift consistently within the concentration range of 0.1–10 pg/mL, which proves the trapping of f-PSA into the nanoledge structure array and plasmonic detection.

In this study, the nanoledge structure topped with SiO_2, which uses transmission SPR light signal transduction for sensing, provides a few advantages over traditional thin film SPR sensors that are based on total internal reflection of light with a prism. Specifically, the SiO_2-topped nanoledge offers a highly sensitive in-cavity detection mode[37] and, meanwhile, avoids the nonspecific binding at the top surfaces. Even though the apparent bulk RI sensitivity (576 nm/RIU for the nanoledge) is smaller than that of traditional thin film SPR (usually thousands nm/RIU), the actual measurable sensitivity for affinity sensing is comparable or higher. This is because the evanescent field of LSPR in the nanoledge has a much shorter decay and stronger near-field enhancement than that of the propagating SPR along the thin film, greatly enhancing the sensitivity in detecting RI changes at the sensing vicinity of the metal/dielectric interface.[52-54] In order to have strong SPR-induced optical transmission for sensing, a narrowed nanoslit (<100 nm) is necessary;[37] however, it limits charged analytes (e.g., proteins) diffusion into the nanoslit due to the overlap of electric double layer effect in the nanochannel.[55, 56] The nanoledge structure, by combining narrow slit at the bottom and the wide open top, not only generates strongly coupled SPR-induced optical transmission, but also overcomes the limit of small (<100 nm) nanochannels for migration of protein analytes into the channel, as shown in the results presented above. Moreover, it is expected that the SiO_2 topped nanoledge structure would not allow large biological species, for example cells, transporting into the ledge sensing area when it is used for protein detection from whole blood or serum samples. This research is underway, and some preliminary results have been obtained.

Conclusions

In summary, we presented a new SiO_2 topped nanoledge aperture structure for nanometric-sized protein trapping and sensing. For the nanoledge structures, we applied the decomposition and quantitative analysis of SP generation by a semianalytical model and numerical simulation of optical transmission spectra and RI sensitivity by a FDTD method, which certificated that nanoledge structure with on-top SiO_2 layer had the potential to be effectively applied in T-SPR for protein detection. Experimentally, TIRF imaging showed that proteins can diffuse into the nanoledge structures (with 280 nm open gap) by using similar size straight nanoslits (100 and 300 nm) to investigate the protein migration behavior. The diffusion of the labeled BSA into the nanostructure was measured by FCS, with the results indicating that BSA molecules undergo Brownian motion and have a diffusion coefficient of approximately 70 $\mu m^2/s$ in the nanoslit

cavity, which agrees with its hydrodynamic radius of 3 nm. Further studies of the protein trapping and potential sensing applications were provided by fabricating a subwavelength nanoledge device and testing the SPR optical transmission shift and RI sensitivity for determining the binding events between the mAb and a cancer biomarker f-PSA in buffer solutions.

Supporting Information

The Supporting Information is available free of charge on the ACS Publications website at https://doi.org/10.1021/acs.analchem.6b04493.

Acknowledgment

J.W., Z.Z., and T.M. acknowledge the financial support from U.S. NSF Grant (#1511194) and UNCG faculty first scholarship. This work was performed at the Joint School of Nanoscience and Nanoengineering (JSNN), a member of Southeastern Nanotechnology Infrastructure Corridor (SENIC), and National Nanotechnology Coordinated Infrastructure (NNCI), which is supported by the National Science Foundation (ECCS-1542174).

References

1. Krishnan, M.; Mojarad, N.; Kukura, P.; Sandoghdar, V. Nature **2010**, 467, 692– 695 DOI: 10.1038/nature09404

2. Zheng, B. Y.; Wang, Y.; Nordlander, P.; Halas, N. J. Adv. Mater. **2014**, 26, 6318– 6323 DOI: 10.1002/adma.201401168

3. Cohen, A. E. Phys. Rev. Lett. **2005**, 94, 118102 DOI: 10.1103/PhysRevLett.94.118102

4. Huang, L. R.; Cox, E. C.; Austin, R. H.; Sturm, J. C. Science **2004**, 304, 987– 990 DOI: 10.1126/science.1094567

5. Singh, P. S.; Kätelhön, E.; Mathwig, K.; Wolfrum, B.; Lemay, S. G. ACS Nano **2012**, 6, 9662– 9671 DOI: 10.1021/nn3031029

6. Cohen, A. E.; Moerner, W. E. Proc. Natl. Acad. Sci. U. S. A. **2006**, 103, 4362– 4365 DOI: 10.1073/pnas.0509976103

7. Krishnan, M.; Mönch, I.; Schwille, P. Nano Lett. **2007**, 7, 1270– 1275 DOI: 10.1021/nl0701861

8. Wenger, J.; Rigneault, H. Int. J. Mol. Sci. **2010**, 11, 206– 221 DOI: 10.3390/ijms11010206

9. Geissbuehler, M.; Bonacina, L.; Shcheslavskiy, V.; Bocchio, N. L.; Geissbuehler, S.; Leutenegger, M.; Märki, I.; Wolf, J.-P.; Lasser, T. Nano Lett. **2012**, 12, 1668– 1672 DOI: 10.1021/nl300070n

10. Foquet, M.; Korlach, J.; Zipfel, W. R.; Webb, W. W.; Craighead, H. G. Anal. Chem. **2004**, 76, 1618– 1626 DOI: 10.1021/ac035088o

11. Gérard, D.; Wenger, J.; Bonod, N.; Popov, E.; Rigneault, H.; Mahdavi, F.; Blair, S.; Dintinger, J.; Ebbesen, T. W. Phys. Rev. B: Condens. Matter Mater. Phys. **2008**, 77, 045413 DOI: 10.1103/PhysRevB.77.045413

12. Mütze, J.; Ohrt, T.; Schwille, P. Laser & Photonics Reviews **2011**, 5, 52– 67 DOI: 10.1002/lpor.200910041

13. Subba-Rao, V.; Hoffmann, P. M.; Mukhopadhyay, A. J. Nanopart. Res. **2011**, 13, 6313– 6319 DOI: 10.1007/s11051-011-0607-5

14. Kelly, C. V.; Wakefield, D. L.; Holowka, D. A.; Craighead, H. G.; Baird, B. A. ACS Nano **2014**, 8, 7392– 7404 DOI: 10.1021/nn502593k

15. Nicoli, F.; Verschueren, D.; Klein, M.; Dekker, C.; Jonsson, M. P. Nano Lett. **2014**, 14, 6917– 6925 DOI: 10.1021/nl503034j

16. Chen, P.; Chung, M. T.; McHugh, W.; Nidetz, R.; Li, Y.; Fu, J.; Cornell, T. T.; Shanley, T. P.; Kurabayashi, K. ACS Nano **2015**, 9, 4173– 4181 DOI: 10.1021/acsnano.5b00396

17. Lee, K.-L.; You, M.-L.; Tsai, C.-H.; Lin, E.-H.; Hsieh, S.-Y.; Ho, M.-H.; Hsu, J.-C.; Wei, P.-K. Biosens. Bioelectron. **2016**, 75, 88– 95 DOI: 10.1016/j.bios.2015.08.010

18. Lee, K.-L.; Chen, P.-W.; Wu, S.-H.; Huang, J.-B.; Yang, S.-Y.; Wei, P.-K. ACS Nano **2012**, 6, 2931– 2939 DOI: 10.1021/nn3001142

19. Emam, A. N.; Mohamed, M. B.; Girgis, E.; Rao, K. V. RSC Adv. **2015**, 5, 34696– 34703 DOI: 10.1039/C5RA01918D

20. Cheng, Z.-Q.; Nan, F.; Yang, D.-J.; Zhong, Y.-T.; Ma, L.; Hao, Z.-H.; Zhou, L.; Wang, Q.-Q. Nanoscale **2015**, 7, 1463– 1470 DOI: 10.1039/C4NR05544F

21. Baba, A.; Tada, K.; Janmanee, R.; Sriwichai, S.; Shinbo, K.; Kato, K.; Kaneko, F.; Phanichphant, S. Adv. Funct. Mater. **2012**, 22, 4383– 4388 DOI: 10.1002/adfm.201200373

22. Malic, L.; Morton, K.; Clime, L.; Veres, T. Lab Chip **2013**, 13, 798– 810 DOI: 10.1039/c2lc41123g

23. Wang, P.; Zhang, L.; Xia, Y.; Tong, L.; Xu, X.; Ying, Y. Nano Lett. **2012**, 12, 3145– 3150 DOI: 10.1021/nl301055f

24. Hill, R. T.; Kozek, K. M.; Hucknall, A.; Smith, D. R.; Chilkoti, A. ACS Photonics **2014**, 1, 974– 984 DOI: 10.1021/ph500190q

25. Knoll, W. Annu. Rev. Phys. Chem. **1998**, 49, 569– 638 DOI: 10.1146/annurev.physchem.49.1.569

26. Lalanne, P.; Hugonin, J. P.; Rodier, J. C. Phys. Rev. Lett. **2005**, 95, 263902 DOI: 10.1103/PhysRevLett.95.263902

27. Kress, S. J. P.; Richner, P.; Jayanti, S. V.; Galliker, P.; Kim, D. K.; Poulikakos, D.; Norris, D. J. Nano Lett. **2014**, 14, 5827– 5833 DOI: 10.1021/nl5026997

28. Cetin, A. E.; Etezadi, D.; Galarreta, B. C.; Busson, M. P.; Eksioglu, Y.; Altug, H. ACS Photonics **2015**, 2, 1167– 1174 DOI: 10.1021/acsphotonics.5b00242

29. Gordon, R.; Sinton, D.; Kavanagh, K. L.; Brolo, A. G. Acc. Chem. Res. **2008**, 41, 1049– 1057 DOI: 10.1021/ar800074d

30. Melikyan, A.; Alloatti, L.; Muslija, A.; Hillerkuss, D.; Schindler, P. C.; Li, J.; Palmer, R.; Korn, D.; Muehlbrandt, S.; Van Thourhout, D.; Chen, B.; Dinu, R.; Sommer, M.; Koos, C.; Kohl, M.; Freude, W.; Leuthold, J. Nat. Photonics **2014**, 8, 229– 233 DOI: 10.1038/nphoton.2014.9

31. Reiner, J. E.; Robertson, J. W. F.; Burden, D. L.; Burden, L. K.; Balijepalli, A.; Kasianowicz, J. J. J. Am. Chem. Soc. **2013**, 135, 3087– 3094 DOI: 10.1021/ja309892e

32. Zeng, Z.; Mendis, M. N.; Waldeck, D. H.; Wei, J. RSC Adv. **2016**, 6, 17196– 17203 DOI: 10.1039/C6RA01105E

33. Zeng, Z.; Liu, Y.; Wei, J. TrAC, Trends Anal. Chem. **2016**, 75, 162– 173 DOI: 10.1016/j.trac.2015.06.009

34. Wei, J.; Rexius, M.; Kofke, M.; Wang, Y.; Singhal, S.; Waldeck, D. H. Nanotechnology **2011**, 3, 79– 82

35. Sanders, M.; Lin, Y.; Wei, J.; Bono, T.; Lindquist, R. G. Biosens. Bioelectron. **2014**, 61, 95– 101 DOI: 10.1016/j.bios.2014.05.009

36. Eftekhari, F.; Escobedo, C.; Ferreira, J.; Duan, X.; Girotto, E. M.; Brolo, A. G.; Gordon, R.; Sinton, D. Anal. Chem. **2009**, 81, 4308– 4311 DOI: 10.1021/ac900221y

37. Lee, K.-L.; Wang, W.-S.; Wei, P.-K. Biosens. Bioelectron. **2008**, 24, 210– 215 DOI: 10.1016/j.bios.2008.03.044

38. Gordon, R.; Brolo, A. G.; McKinnon, A.; Rajora, A.; Leathem, B.; Kavanagh, K. L. Phys. Rev. Lett. **2004**, 92, 037401 DOI: 10.1103/PhysRevLett.92.037401

39. Escobedo, C.; Brolo, A. G.; Gordon, R.; Sinton, D. Anal. Chem. **2010**, 82, 10015– 10020 DOI: 10.1021/ac101654f

40. Lalanne, P.; Hugonin, J. P.; Rodier, J. C. J. Opt. Soc. Am. A **2006**, 23, 1608– 1615 DOI: 10.1364/JOSAA.23.001608

41. Vial, A.; Laroche, T. Appl. Phys. B: Lasers Opt. **2008**, 93, 139– 143 DOI: 10.1007/s00340-008-3202-4

42. Aouani, H.; Wenger, J.; Gérard, D.; Rigneault, H.; Devaux, E.; Ebbesen, T. W.; Mahdavi, F.; Xu, T.; Blair, S. ACS Nano **2009**, 3, 2043– 2048 DOI: 10.1021/nn900460t

43. Shi, X.; Li, X.; Kaliszewski, M. J.; Zhuang, X.; Smith, A. W. Langmuir **2015**, 31, 1784– 1791 DOI: 10.1021/la504241w

44. Shi, X.; Kohram, M.; Zhuang, X.; Smith, A. W. Langmuir **2016**, 32, 1732– 1741 DOI: 10.1021/acs.langmuir.5b02814

45. Petrášek, Z.; Schwille, P. Biophys. J. **2008**, 94, 1437– 1448 DOI: 10.1529/biophysj.107.108811

46. De Santo, I.; Causa, F.; Netti, P. A. Anal. Chem. **2010**, 82, 997– 1005 DOI: 10.1021/ac902270k

47. González Flecha, F. L.; Levi, V. Biochem. Mol. Biol. Educ. **2003**, 31, 319– 322 DOI: 10.1002/bmb.2003.494031050261

48. Jung, L. S.; Campbell, C. T.; Chinowsky, T. M.; Mar, M. N.; Yee, S. S. Langmuir **1998**, 14, 5636– 5648 DOI: 10.1021/la971228b

49. Haemers, S.; Koper, G. J. M.; van der Leeden, M. C.; Frens, G. Langmuir **2002**, 18, 2069– 2074 DOI: 10.1021/la010506a

50. Chen, S.; Svedendahl, M.; Käll, M.; Gunnarsson, L.; Dmitriev, A. Nanotechnology **2009**, 20, 434015 DOI: 10.1088/0957-4484/20/43/434015

51. Mulder, S. D.; Heijst, J. A.; Mulder, C.; Martens, F.; Hack, C. E.; Scheltens, P.; Blankenstein, M. A.; Veerhuis, R. Ann. Clin. Biochem. **2009**, 46, 477– 483 DOI: 10.1258/acb.2009.009130

52. Yonzon, C. R.; Jeoung, E.; Zou, S.; Schatz, G. C.; Mrksich, M.; Van Duyne, R. P. J. Am. Chem. Soc. **2004**, 126, 12669– 12676 DOI: 10.1021/ja047118q

53. Haes, A.; Duyne, R. Anal. Bioanal. Chem. **2004**, 379, 920– 930 DOI: 10.1007/s00216-004-2708-9

54. Lee, K.-L.; Chang, C.-C.; You, M.-L.; Pan, M.-Y.; Wei, P.-K. Sci. Rep. **2016**, 6, 33126 DOI: 10.1038/srep33126

55. Pennathur, S.; Santiago, J. G. Anal. Chem. **2005**, 77, 6772– 6781 DOI: 10.1021/ac050835y

56. Karnik, R.; Fan, R.; Yue, M.; Li, D.; Yang, P.; Majumdar, A. Nano Lett. **2005**, 5, 943– 948 DOI: 10.1021/nl050493b